Available online at www.sciencedirect.com
ScienceDirect
Aerosol Science 39 (2008) 253–265
Journal of Aerosol Science
www.elsevier.com/locate/jaerosci

Numerical study of fibre deposition in a human nasal cavity

Kiao Inthavong, Jian Wen, Zhaofeng Tian, Jiyuan Tu*

School of Aerospace, Mechanical and Manufacturing Engineering, RMIT University, PO Box 71, Plenty Road, Bundoora, Vic. 3083, Australia

Received 24 May 2007; received in revised form 1 November 2007; accepted 13 November 2007

Abstract

The inhalation of toxic particles such as asbestos fibres through the nasal airway has been found to cause harmful damage to the respiratory system. This study made use of CFD techniques to investigate deposition of fibrous particles in a human nasal cavity. A 3D computational model was created from CT scans which provided the framework to study the flow and deposition of fibres at a constant flow rate of 7.5 L/min. The effects of the fibres' elongated shape, density and size were incorporated into empirical drag correlations and the fibre trajectories were recorded through a Lagrangian tracking scheme. In general, good agreement was found in the right cavity and an overprediction in the left cavity. The major cause of deposition differences was in the geometrical variations between subjects as well as the left and right cavities. The dominant mechanism of deposition was by inertial impaction, with a majority of the particles depositing in the anterior region. It was found that asbestos had a very low deposition, $\approx 14\%$, and was independent of fibre length. In comparison, the carbon fibre exhibited increases in deposition as the fibre length increased. A parameter ρA_{cross} which represents the mass per unit length was used to equate the d_{ae} for different fibre lengths.

Keywords: Nasal airway; Fibre; Morphology; CFD; Deposition

1. Introduction

The inhalation of toxic particles through the nasal airway has been found to cause adverse health responses (Balásházy, Hofmann, & Heistracher, 2003; Kreuzer et al., 2000). Inhalation of fibrous materials, such as asbestos, is one case that has been identified in the workplace. Asbestos (Fig. 1) was once popular among manufacturers and builders in the late 19th century due to its resistance to heat, sound absorption and tensile strength. However, since the inhalation of asbestos fibres was found to cause serious illnesses such as asbestosis and mesothelioma, the use of asbestos was banned in many countries. Despite this, the risk of exposure still exists mainly through the demolition of older buildings and materials where the fibres become airborne. An alternative for asbestos fibres is the use of man-made vitreous fibres (MMVFs) using inorganic materials such as glass, natural rock and amorphous silicates. MMVFs themselves are not free from toxic properties. The levels of toxicity vary and this is dependent on the fibre length and their biopersistence in the lungs (Lippman, 1990; Timbrell, 1982).

Currently there are very few studies that have investigated fibre deposition in the human nasal airway. Using carbon fibres with a uniform diameter and polydisperse length, Su and Cheng (2005) investigated the deposition patterns in the nasal cavity at different constant flow rates. It was found that impaction was the dominant deposition mechanism and

* Corresponding author. Tel.: +61 3 9925 6191; fax: +61 3 9925 6108.
E-mail address: jiyuan.tu@rmit.edu.au (J. Tu).

0021-8502/$ - see front matter © 2007 Elsevier Ltd. All rights reserved.
doi:10.1016/j.jaerosci.2007.11.007

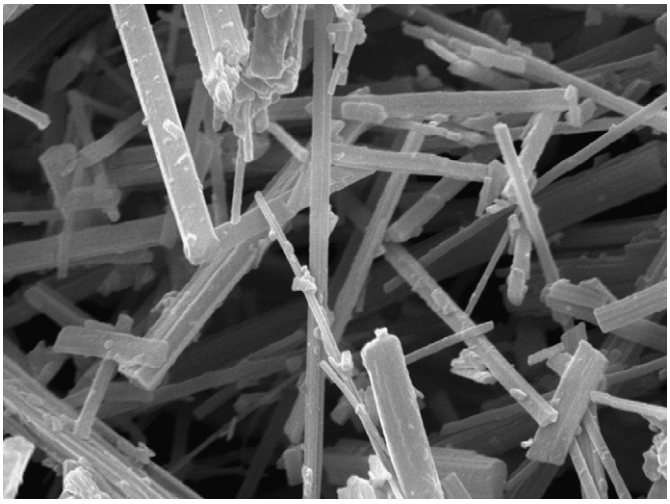

Fig. 1. Electron microscope image amosite asbestos. (Photograph courtesy of the US Geological Survey—www.usgs.gov).

most of the fibres with high inertia deposited in the anterior region of the nasal cavity (vestibule and nasal valve region). The results obtained by Su and Cheng (2005) provide important experimental data; however, due to the nature of in vivo methods, fine quantitative details are not possible. The use of computational fluid dynamics (CFD) techniques presents an alternative to produce data that can complement existing experimental data. It is an attractive method that is cost-effective, enables enormous amounts of precise data and has the ability to provide deeper insight into the nature of nasal airflow. For example, CFD simulations for airflow patterns (Finck, Hänel, & Wlokas, 2006; Keyhani, Scherer, & Mozell, 1995; Subramaniam, Richardson, Morgan, & Kimbell, 1998) have complemented experimental results (Hahn, Scherer, & Mozell, 1993) by confirming regions of vortices within the nasal vestibule, the olfactory region and the nasal valve. Simulations for particle deposition, however, are fewer in numbers. Inthavong et al. (2006) studied spherical particle deposition under conditions related to pharmaceutical nasal spray applications. Particles in the range of 10 to 50 μm subjected to a breathing flow rate of 20 L/min resulted in a large proportion of particles being deposited in the anterior third of the nasal cavity, which were attributed to the injected particles existing in a high inertial regime. On the other hand, Zamankhan et al. (2006) simulated the deposition of nano-sized particles in the nasal cavity under steady laminar conditions where diffusion was the dominant deposition mechanism for the smallest range of particles (1–30 nm). In both cases the effects of particle morphology were not included. Clearly, fibres with their elongated form exhibit vastly different aerodynamic properties in comparison with spherical particles. Crowder, Rosati, Schroeter, Hickey, and Martonen (2002) point out the importance of particle morphology in the deposition of particles in the lungs by citing the significance of particle density, shape, size and surface characteristics (roughness, vapour pressure, etc.).

Therefore, this study made use of CFD techniques to investigate deposition of fibrous particles in a human nasal cavity. The effects of the fibres' elongated shape, density and size were incorporated into empirical drag correlations and the fibre trajectories recorded through a Lagrangian tracking scheme. Detailed data were obtained which serve to complement existing experimental data. The effects of the airway geometry on the airflow and finally on the deposition patterns were also investigated to further understand fibre flow dynamics within the airway.

2. Methods

2.1. CT scanning

A nasal cavity geometry was obtained through a computed tomography (CT) scan of the nose of a healthy 25 year old Asian male (170-cm height, 75 kg mass). The CT scan was performed using a CTI whole body scanner (General Electric). The single-matrix scanner was used in helical mode with 1-mm collimation, a 40-cm field of view, 120 kV peak and 200 mA. The scans captured outlined slices in the X–Y plane at different positions along the Z-axis from the entrance of the nasal cavity to just anterior of the larynx at intervals of 1–5 mm depending on the complexity of

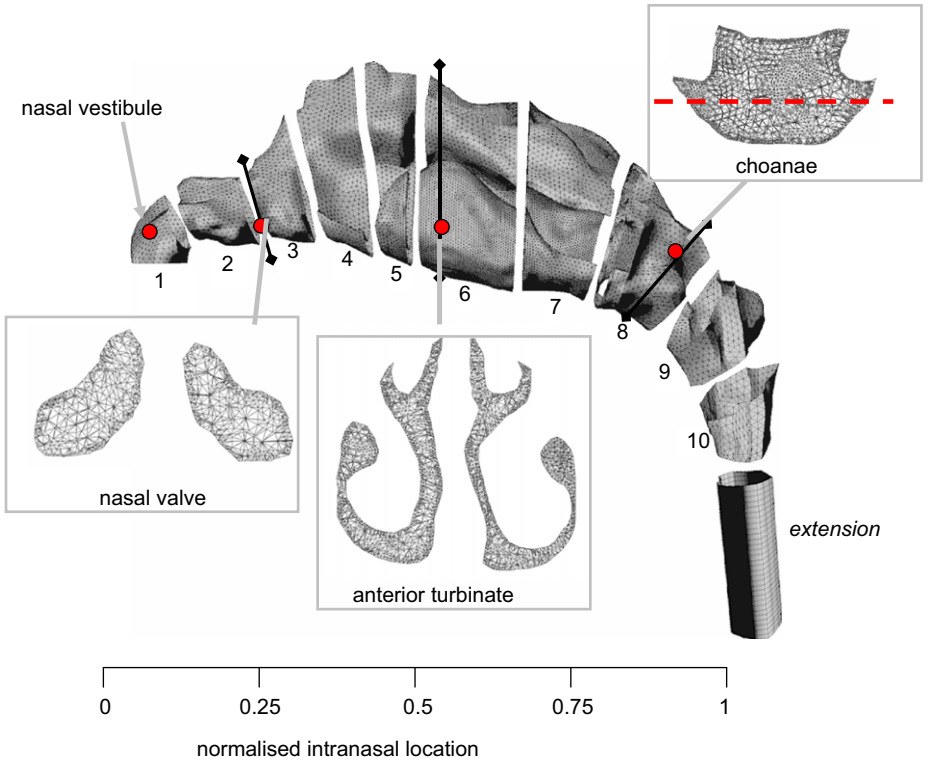

Fig. 2. Computational model with 950,000 cells subdivided into 10 regions to represent local deposition regions. Three cross-sections display the internal mesh where the dashed line across at the posterior end of the nasal cavity (choanae) is used for grid independence in Fig. 3.

the anatomy. The coronal sectioned scans were imported into a 3D modelling program called GAMBIT which created smooth curves that connected points on the coronal sections. Surfaces were then created and stitched up to create a computational mesh. An initial model with 82,000 cells was created and used to solve the airflow field at a flow rate of 10 L/min. The original model was refined by cell adaptation techniques that included refining large volume cells, cells that displayed high velocity gradients and near wall refinements. This process was repeated twice, with each repeat producing a model with a higher cell count than the previous model. Subsequently, four models were produced: 82,000, 586,000, 950,000 and 1.44 million cells. A model containing 950,000 cells is shown in Fig. 2 with three coronary slices showing the internal mesh with a dense region near the walls. A grid independence test (Fig. 3) found that the results for average velocity taken along a line at the posterior end of the nasal cavity from Fig. 2 converge around 950,000 cells.

2.2. *Fluid flow modelling*

Due to the complex geometry of the anatomically real nasal cavity, a commercial CFD code, FLUENT, was utilised to predict the continuum air phase flow through solutions of the conservation equations of mass and momentum. These equations were discretised using the finite volume approach. The third order accurate QUICK scheme was used to approximate the momentum equation whilst the pressure–velocity coupling was realised through the SIMPLE method. To be consistent with experimental data, a constant flow rate of 7.5 L/min was used to simulate light breathing. At this flow rate, the flow regime has been determined to be laminar (Hahn et al., 1993; Swift & Proctor, 1977). A steady flow rather than a cyclic unsteady flow was used in this case to allow the results to emphasise the effects of particle morphology on deposition sites independent of cyclic conditions. Moreover, the effects of a periodic inhalation on the overall flow field are found to be negligible from the Womersley frequency variable which is used to determine the importance of the fluctuating sinusoidal pattern of the inhalation–exhalation breathing cycle. The calculated Womersley

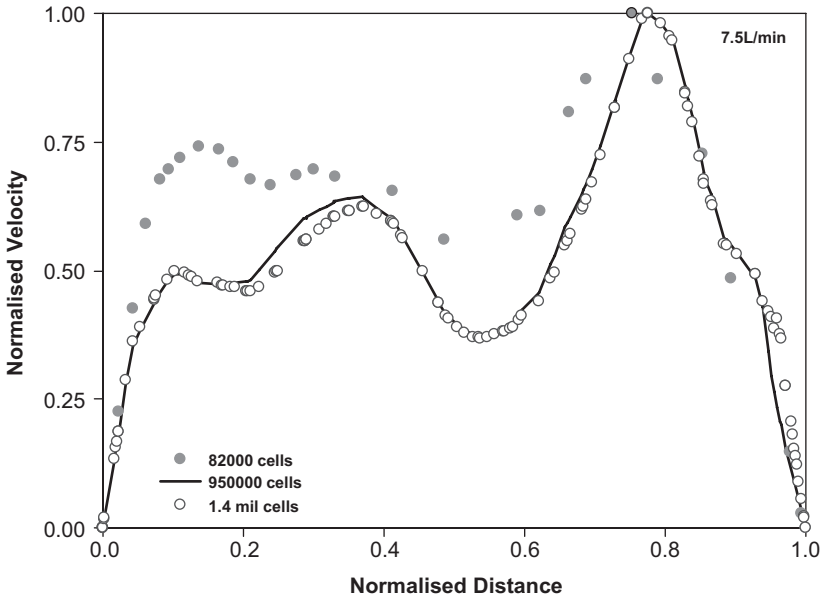

Fig. 3. Grid independence test based on a velocity profile line taken at the posterior end of the nasal cavity from Fig. 2. The distance and velocities are normalised by their respective maximum values of $x_{max} = 96.5$ cm and $U_{max} = 1.36$ m/s.

frequency variable

$$W = \frac{D}{2}\left(\frac{\omega}{v_g}\right)^{0.5} \tag{1}$$

was 0.3 where D is the local cross-sectional distance between the two nasal walls and is about 0.5 cm in this nasal cavity, v_g is the kinematic viscosity of air and ω is the breathing frequency. The steady-state continuity and momentum equations for the air phase in Cartesian tensor notation are

$$\frac{\partial}{\partial x_i}(\rho_g u_i^g) = 0, \tag{2}$$

$$\rho u_j^g \frac{\partial u_i^g}{\partial x_j} = -\frac{\partial p_g}{\partial x_i} + \frac{\partial}{\partial x_j}\left(\mu_g \frac{\partial u_i^g}{\partial x_j}\right), \tag{3}$$

where u_i^g is the ith component of the time averaged velocity vector and ρ_g is the air density.

2.3. Particle trajectory modelling

A Lagrangian particle tracking method is used to trace the dispersion of particle about its trajectory. The Lagrangian scheme is most popular in engineering applications for the prediction of particle flows for its ability to track individual particles. Trajectories of individual particles can be tracked by integrating the force balance equations on the particle:

$$\frac{du_p}{dt} = F_D(u_g - u_p) + \frac{g(\rho_p - \rho_g)}{\rho_p}, \tag{4}$$

where u_p is the particle velocity and ρ_p is the particle density. It is noted that the gravity term, 'g', was taken as -9.81 m/s^2 taken in the Y-axis and hence is applicable for an upright position. Additional source terms for the particle equation such as Brownian force are not included as the particles concerned are substantially greater than submicron particles that are influenced by their mean free path. Additionally, the particles are far denser than air, causing terms

that depend on the density ratio, such as the pressure force, buoyancy force, virtual mass effect and Basset force, to be very small. The drag force per unit particle mass is $F_D(u_g - u_p)$ and F_D is given by

$$F_D = \frac{18\mu_g}{\rho_p d_p^2}\frac{C_D Re_p}{24}, \tag{5}$$

where d_p is the particle volume equivalent diameter and μ_g is the molecular viscosity of the fluid. Re_p is the particle Reynolds number, which is defined as

$$Re_p \equiv \frac{\rho_p d_p |u_p - u_g|}{\mu_g}. \tag{6}$$

2.4. Drag correlations for irregular shapes

The drag force is related to the drag coefficient which has been studied quite extensively. The general correlation for smooth spherical particles is given by Clift, Grace, and Weber (1978):

$$C_D = \frac{24}{18} Re_p (18 + 2.367\, Re_p^w) \quad \text{for } Re < 20, \tag{7}$$

$$w = 0.82 - 0.05(\log_{10} Re_p).$$

For non-spherical particles such as fibres, considerable developments in formulating a single correlation for arbitrary shapes have been performed. One well-known correlation is by Haider and Levenspiel (1989) which will be referred to as the HL-model. Their correlation defines the C_D as a function of the particle Reynolds number and a shape factor which is given as

$$C_D = \frac{24}{Re_p}(1 + aRe_p^b) + \frac{cRe_p}{d + Re_p}, \tag{8}$$

where

$$a = \exp(2.3288 - 6.4581\phi + 2.4486\phi^2),$$

$$b = 0.0964 + 0.5565\phi,$$

$$c = \exp(4.905 - 13.8944\phi + 18.4222\phi^2 - 10.2599\phi^3),$$

$$d = \exp(1.4681 + 12.2584\phi - 20.7322\phi^2 + 15.8855\phi^3)$$

and the shape factor ϕ is defined as

$$\phi = \frac{A_s}{A_p}, \tag{9}$$

where A_s is the surface area of a sphere having the same volume as the particle and A_p is the actual surface area of the particle.

It has been reported that the accuracy of the HL-model decreases as the shape factor decreases (Gabitto & Tsouris, 2007). A different and novel approach is by Tran-Cong, Gay, and Michaelides (2004) which defines the fibre by spherical aggregate particles clustered into a cylindrical bar configuration. This correlation will be referred to as the TC-model. Two equivalent diameters and a shape factor called the 'degree of circularity' (Wadell, 1933) are used for the drag correlation. The volume equivalent sphere diameter, also known as the nominal diameter, is defined as

$$d_n = \sqrt[3]{6V/\pi}, \tag{10}$$

where V is the particle volume. The surface equivalent sphere diameter is defined as

$$d_A = \sqrt{4A_{proj}/\pi}, \tag{11}$$

Table 1
Summary of fibre morphological characteristics, typical mean values and numerical models (Haider & Levenspiel, 1989; Su & Cheng, 2005; Tran-Cong et al., 2004; WHO, 2000)

Shape	Typical size range	Density	Real Image	Modelling Techniques
Elongated cylinders	**Asbestos Fibre** Diameter (FD) < 3 μm	**Asbestos** 260-400 kg/m^3	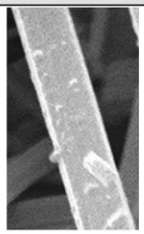 *Photograph Courtesy of the U.S. Geological Survey*	*Elongated cylinder method by Haider and Levenspiel (1989)* 
	Carbon Fibre Diameter (FD) ≈ 2-15 μm *Su and Cheng (2005)*	**Carbon** 1830kg/m^3 *Su and Cheng (2005)*		
	Fibre Length (FL) > 5 μm **Aspect Ratio** $\beta = \frac{FL}{FD} > 3$ *WHO (2000)*			*Clusters of spherical aggregate particles by Tran-Cong et al. (2004)* 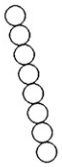

where A_{proj} is the projected area of the sphere. The circularity is defined as

$$c = \pi(d_A / P_{\text{proj}}), \tag{12}$$

where P_{proj} is the projected perimeter of the particle in its direction of motion.

The empirically defined correlation for the drag coefficient is given as

$$C_{\text{D}} = \frac{24}{Re_{\text{p}}}\frac{d_A}{d_{\text{n}}}\left[1 + \frac{0.15}{\sqrt{c}}\left(\frac{d_A}{d_{\text{n}}}Re_{\text{p}}\right)^{0.687}\right] + \frac{0.42(d_A/d_{\text{n}})^2}{\sqrt{c}[1 + 42,500((d_A/d_{\text{n}})Re_{\text{p}})^{-1.16}]}. \tag{13}$$

The correlation was implemented into FLUENT via the user-defined function allowing a customised drag correlation. Table 1 summarises the fibres' morphological characteristics, typical mean values and numerical models to account for the elongated shape.

3. Results and discussion

3.1. Carbon fibre deposition

Monodisperse carbon fibres with a diameter of 3.66 mm, density at 1.83 g/cm^3 and varying lengths were simulated through the left and right nasal cavities at a flow rate of 7.5 L/min. The two approaches, the HL-model and the

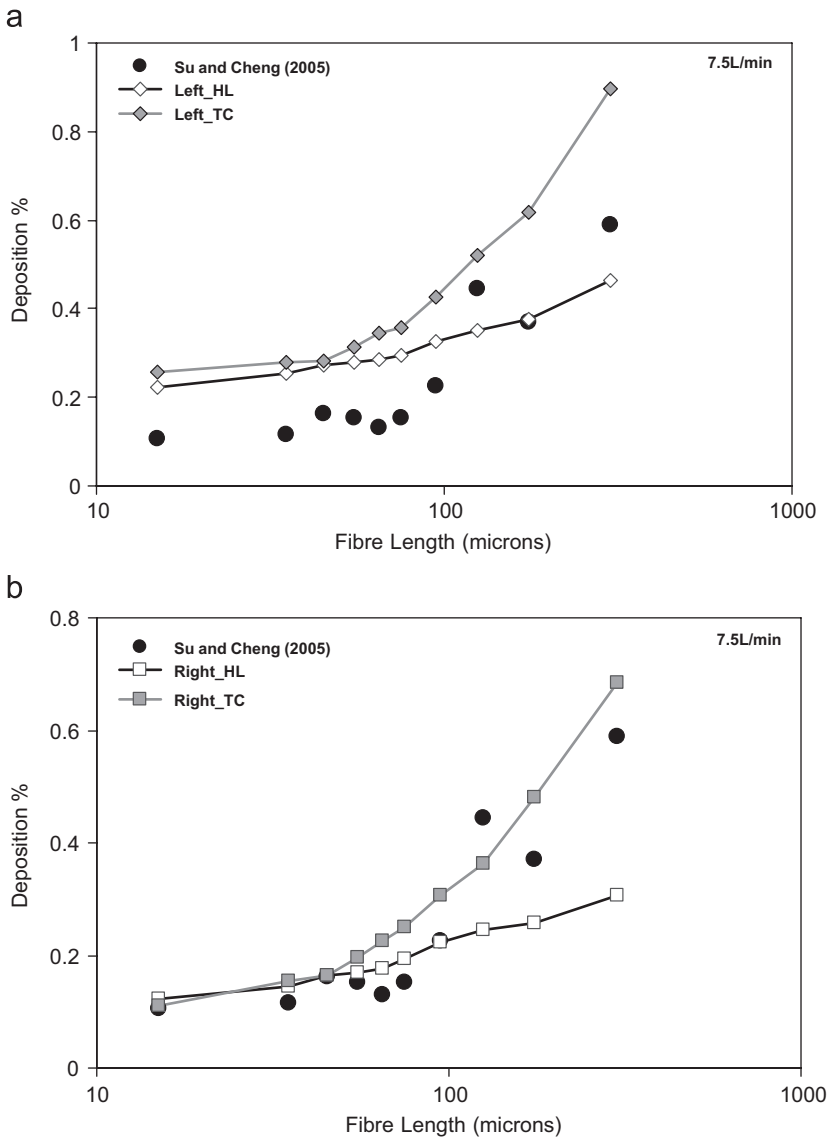

Fig. 4. Fibre deposition comparison in the cavity using the two different drag correlations, the HL-model and the TC-model, against the experimental data.

TC-model, in modelling the aerodynamic flight of the fibres were used. The simulation found close agreement between the experimental data with the deposition values of the cavity using the TC-model (Fig. 4). At short fibre lengths the deposition differences between the two models are similar while for long fibre lengths a difference of 37% is observed. The differences between the two models are consistent and it is the handling of the drag coefficient through the model correlations that provides the variances in the particle trajectory. The HL-model uses a shape factor to define the fibre elongation where, according to its definition (Eq. (8)), the shape factor of a sphere is equal to 1. The greater the aspect ratio and hence the greater length to diameter ratio, the lower the shape factor becomes. For isometrically shaped particles the shape factor is considered the best single parameter for describing the shape of falling particles; however, at low shape factors, the accuracy becomes compromised (Haider & Levenspiel, 1989). On the other hand, the TC-model uses a circularity parameter that has the advantage of allowing the correlation of flow dependence on particle orientation (Eq. (13)). The other major cause of deposition differences is in the nasal geometry variations between subjects as well as the differences in left and right cavities. This factor is discussed in the following sections.

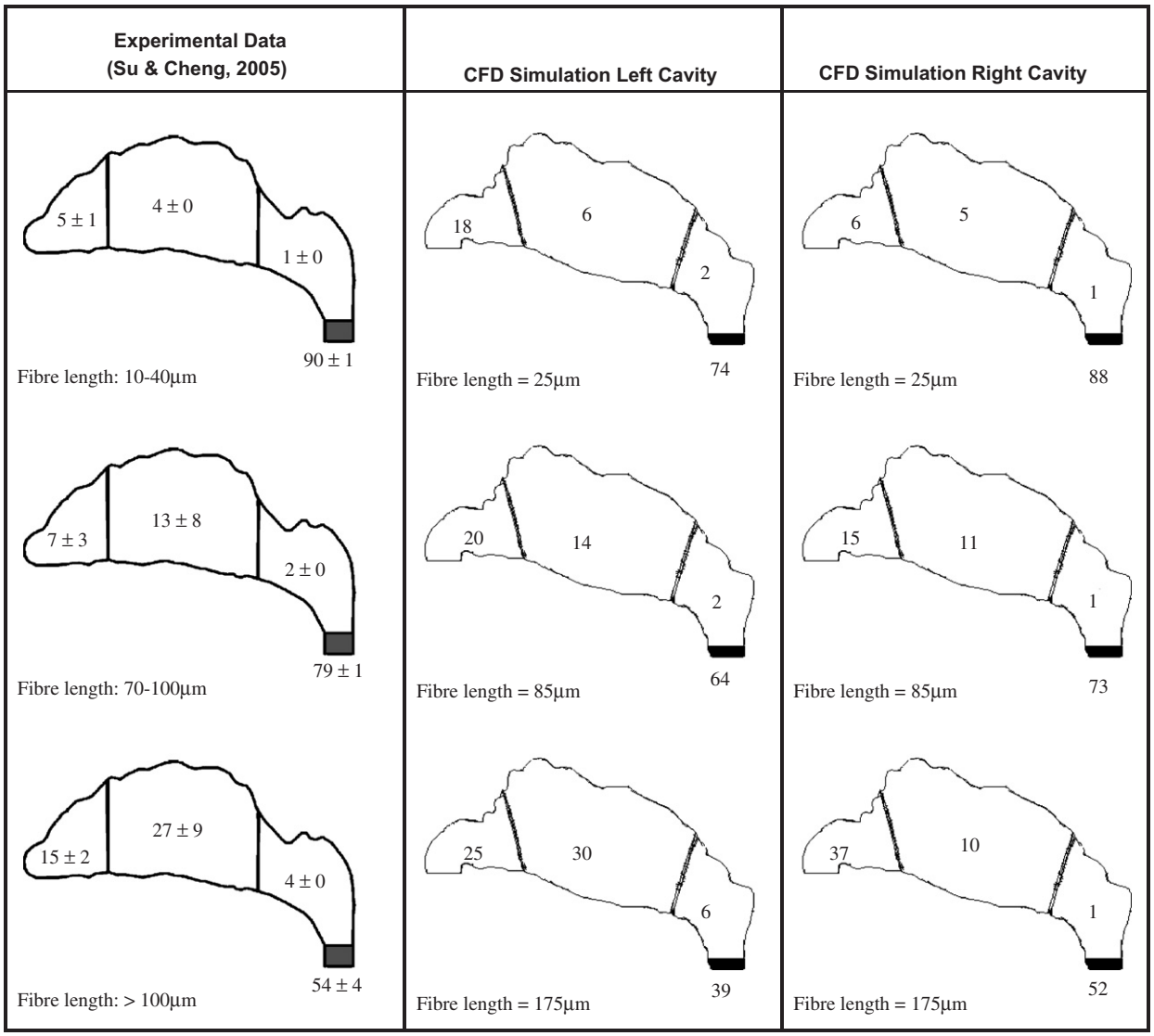

Fig. 5. Fibre deposition patterns for an inspiratory flow rate of 7.5 L/min. Deposition fractions for each region are shown as percentages.

The drag coefficient is intrinsically linked to the particle Reynolds number (Re_p). Given that the particle shape is the controlled variable, it is the slip velocity attained through the aerodynamic flight of the particles in relation to the fluid path that is the deterministic cause of Re_p. For the velocity (10^1), particle size (10^{-6}) and viscosity ($1/10^{-6}$) scales involved, the calculated Re_p are in the range of 0.02–1. A longer fibre length causes greater elongation and therefore the drag coefficient increases due to the non-spherical shape. For long fibre lengths the shape factor and circularity values decrease. The differences between the two models are greatest at the longest fibre lengths where the empirical correlations become less accurate. At shorter lengths the models have closer agreement with each other and provide more accurate data fits (Haider & Levenspiel, 1989).

3.1.1. Carbon fibre deposition comparisons

The deposition fractions for the front, middle and back regions of the left and right nasal cavities were obtained and compared with experimental data (Su & Cheng, 2005) from a different airway model (Fig. 5). The deposition patterns indicate that most of the fibres pass through the nasal cavity, potentially reaching the lungs. The number of fibres

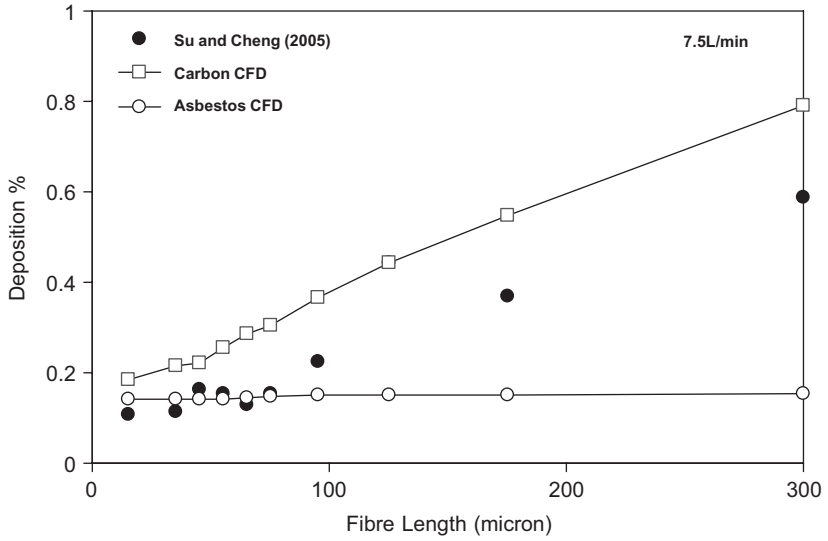

Fig. 6. Total deposition efficiency for asbestos and carbon fibres at different fibre lengths.

passing through the cavities decreases as the fibre length increases implying that longer fibres enhance the deposition. As discussed earlier, the left cavity shows greater deposition, while the right cavity produced more similar results to the experimental data. In nearly all the cases, deposition is dominant in the anterior regions. This region is characterised by the convergent–divergent shape of the nasal valve. The narrowing anterior nasal valve accelerates the bulk flow through the cross-sectional centres while localised pockets of low-flow regions form around it. Posterior to the nasal valve the airway diverges and expands causing a favourable pressure gradient that induces flow separation and vortices. The nasal valve region causes violent flow patterns that enhance the fibre deposition. The middle regions generally exhibit lower deposition except for the case with fibre lengths equal to 175 μm in the left cavity.

3.1.2. Asbestos fibre deposition

Typical values for carbon and asbestos fibres found in literature are summarised in Table 1. The toxicity of the fibres has been linked to its length where fibre deposition in the lungs can be carcinogenic. The CFD simulated deposition values shown in Fig. 6 are the average depositions from the left and right cavities. The effects of fibre length on the two fibre types are markedly different. Deposition of asbestos fibres in the nasal airway is low and exhibits little variation despite the significant variation in length. The low deposition rates (14%) suggest that inhalation of the asbestos fibres will lead to deep respiratory deposition such as the lungs. In contrast, the carbon fibres increase from 18% to 80% in deposition as the fibre length increases from 10 to 300 μm. The cross-sectional diameter of the carbon fibres is approximately three times that of asbestos while the density is six times as great. The length of carbon therefore becomes more significant due to a greater mass per unit length.

The deposition patterns produced for the two different fibres show very sparse deposition for asbestos (Fig. 7). The main deposition regions for both fibre types are found in the middle airway at the inner septum walls and also at the back region at the nasopharynx region. High deposition is also found near the nasal valve region where flow acceleration and deceleration occur. Due to the Lagrangian tracking methodology, the deposition sites shown consider only particle deposition by inertial impaction, where it was found by Su and Cheng (2005) that fibre deposition in the nasal airway is mainly due to impaction and that short fibres could have the same deposition fraction as long fibres in a specific nasal airway region or subregion, as long as the inertial parameters for both fibres are in the same range. However, for asbestos ($d_{ae} \approx 1$ μm) at low flow rates such as 7.5 L/min the inertial parameter is low and deposition by interception may have a slight increase for very long fibre lengths. Deposition by interception can occur if the particle travels close enough to a surface of the airway passages where an edge of the particle touches the surface. Usually the fibre length determines whether the particle will be intercepted. Typical fibres with a diameter of 1 μm and a length of 200 μm have been found to deposit in the bronchial tree (Sussman, Cohen, & Lippmann, 1991). Although the nasal airway is more

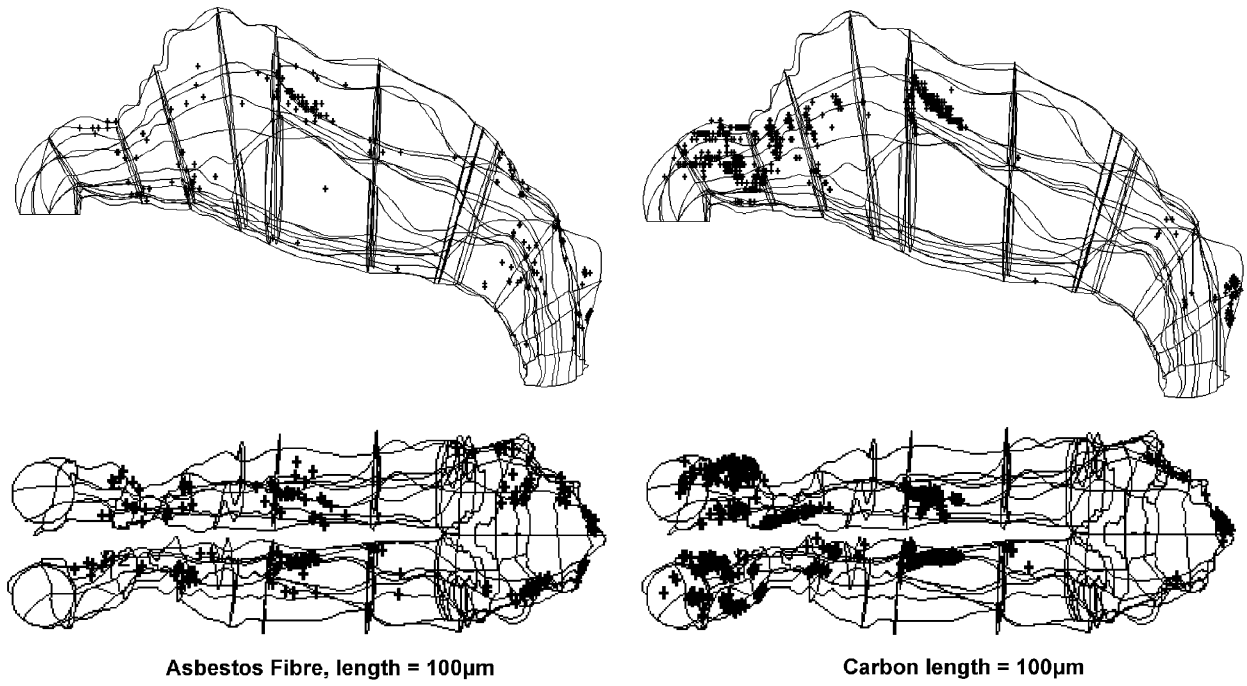

Fig. 7. Deposition patterns for asbestos fibres and carbon fibres at a fibre length of 100 μm at a flow rate of 7.5 L/min.

treacherous in comparison to the tracheobronchial airway, the nose is much larger in size and the effects of deposition of long fibre lengths would be marginal.

3.1.3. Comparison of fibre and spherical particle deposition

Normalisation of the fibres can be performed through Stöber (1972) correlation for an equivalent aerodynamic diameter (d_{ae}) given as

$$d_{ae} = d_{ve}\sqrt{\rho/(1000 \cdot \kappa)}, \tag{14}$$

where d_{ve} is the volume equivalent diameter, ρ is the density of the fibre and κ is the dynamic shape factor for a prolate spheroid. The dynamic shape factor taking the length oriented perpendicular to the flow is given as

$$\kappa_{\perp} = \frac{(8/3)(\beta^2-1)\beta^{1/3}}{\left((2\beta^2-3)/\sqrt{\beta^2-1}\right)\ln\left(\beta+\sqrt{\beta^2-1}\right)+\beta} \tag{15}$$

and also for the length oriented parallel to the flow is given as

$$\kappa_{||} = \frac{(4/3)(\beta^2-1)\beta^{1/3}}{\left((2\beta^2-1)/\sqrt{\beta^2-1}\right)\ln\left(\beta+\sqrt{\beta^2-1}\right)-\beta}, \tag{16}$$

where β is the aspect ratio and is defined as the ratio of the fibre length to the diameter.

For random orientation of the fibre, the shape factor is a combination of the two orientations and is given as

$$\frac{1}{\kappa_R} = \frac{1}{3\kappa_{||}} + \frac{2}{3\kappa_{\perp}}. \tag{17}$$

Taking the random orientation for the dynamic shape factor, the equivalent aerodynamic diameter range for carbon fibre is 7.6–12.8 μm for lengths of 10–300 μm, respectively. For asbestos fibres at the same length range, the d_{ae} range

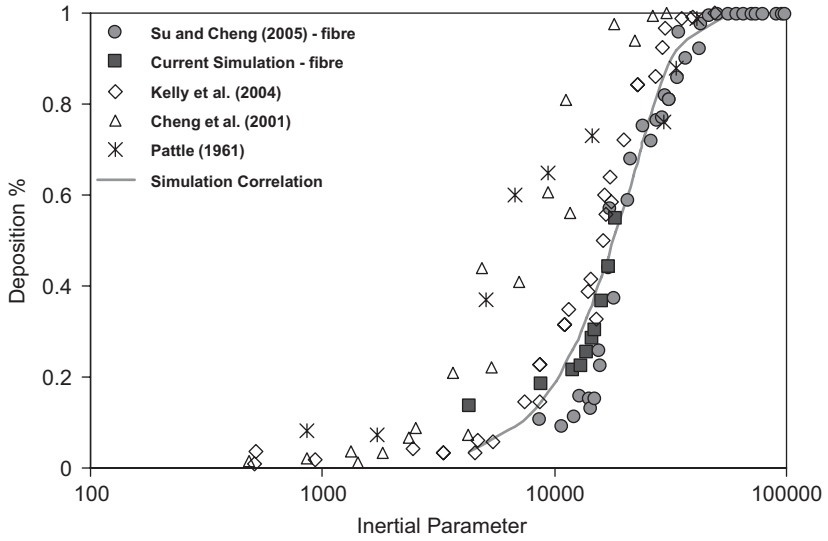

Fig. 8. Comparison of deposition efficiencies between fibres and spherical particles using the inertia parameter.

is 1.0–1.6 μm. This is due to the properties of asbestos exhibiting a light density and small cross-sectional diameter causing the d_{ae} to be independent of its length.

The deposition of the carbon and asbestos fibres over a range of the inertial parameter,

$$\mathrm{IP} = d_{ae}^2 Q, \tag{18}$$

where d_{ae} is the equivalent aerodynamic diameter and Q is the flow rate, is used to compare against previous studies of total deposition efficiencies of monodispersed spherical particles over the nasal cavity as an entire unit Fig. 8 (Pattle, 1961). The inertial parameter is ideal for normalising particle deposition that is dominated by impaction. The deposition efficiency increases as the inertial parameter increases. The range in which the deposition efficiency reaches 90% or more is from 20,000 (Cheng et al., 2001) to 50,000 (Su & Cheng, 2005). The simulation results used the TC-model and show the combined deposition efficiency for the left and right cavity. For IP $< 10,000$ the deposition efficiency is higher for the simulation than for Su and Cheng (2005). The higher values for the smaller inertial particles may be improved by the addition of a wall roughness model (Shi, Kleinstreuer, & Zhang, 2006). An empirical correlation by Kelly, Asgharian, Kimbell, and Wong (2004) to curve fit their experimental data was given as

$$\eta = 1 - \exp(-(\alpha \cdot d_{ae}^2 Q)^{\beta}), \tag{19}$$

where the coefficients are $\alpha = 5.86\mathrm{e} - 5$ and $\beta = 2.1892$.

Similarly, a correlation for the fibre deposition efficiency was found using Matlab R2006b software to program the Levenberg–Marquardt algorithm for constant determination. The coefficients for the correlation given in Eq. (19) are

$$\alpha = 4.654\mathrm{e} - 5, \quad \beta = 2.05.$$

The deposition efficiency curves help to predict the deposition for a given aerodynamic diameter and flow rate. With the production of man-made fibres, there is an opportunity to control properties of the fibre that may lead to adverse health effects such as the fibre length. In the case of carbon fibres, the longer fibre lengths helped increase deposition within the nasal cavity thereby reducing the potential deep lung inhalation. Conversely, deposition of asbestos fibres was found to be independent of their lengths given the lighter density and smaller diameters. By taking the product of the density with the cross-sectional area, the parameter of mass per unit length,

$$\rho A_{\mathrm{cross}}\ \mathrm{kg/m} \tag{20}$$

Table 2
A comparison of particle deposition efficiency for asbestos, carbon fibre and other arbitrary fibres with varying ρA_{cross} values

	Density (kg/m^3)	Diameter (μm)	ρA_{cross} (kg/m)	Length (μm)	d_{ae} (μm)	Equivalent d_{ae} total deposition (%)
Asbestos	300	1	300	10	1.09	0.00
				100	1.44	0.01
				300	1.59	0.02
Carbon fibre	1830	3.66	19,390	10	7.60	10.1
				100	11.3	42.8
				300	12.8	60.1
Fibre 1	1000	3.56	10,000	10	5.49	2.8
				100	8.20	13.5
				300	9.25	21.2
Fibre 2	3190	4	40,000	10	10.69	35.1
				100	16.18	90.7
				300	18.3	98.1

is used to define the resulting d_{ae}. Table 2 shows the significance of the fibre lengths on the effects of d_{ae} for different ρA_{cross} values. The deposition of the fibres can then be predicted by using the resultant d_{ae} for the fibre in question and applying the deposition efficiency curve correlation (Eq. (19)). The ρA_{cross} value for asbestos and carbon fibre is 300 and 19,390, respectively. As ρA_{cross} increases, d_{ae} increases as expected but is most significant in the smaller length range.

4. Conclusion

The inhalation of toxic particles through the nasal airway has been found to cause adverse responses, especially fibres such as asbestos. A 3D computational model was created from CT scans which provided the framework to study deposition of fibres. The effects of a fibre's elongation were accounted for through two different empirically defined drag correlations. At a flow rate of 7.5 L/min the fibre deposition was compared with experimental data. In general, it showed reasonable agreement in the right cavity and an overprediction in the left cavity. Differences were found between the empirical models which were mainly attributed to the way the fibre's non-sphericity was defined such as the shape factor or degree of circularity. The other major cause of deposition differences was in the geometrical variations between subjects as well as the left and right cavities. The airflow analysis showed vortices present in the nasal valve region which enhanced fibre deposition by trapping and recirculating the fibre in the regions where the axial velocity is low. The dominant mechanism of deposition was by inertial impaction, with a majority of the particles depositing in the anterior region. For impaction, the inertial parameter is a useful tool that allows comparisons between particles that exist in this inertial framework. It was found that asbestos had a very low deposition, $\approx 14\%$, and was independent of fibre length. In comparison, the carbon fibre exhibited increases in deposition as the fibre length increased. A parameter ρA_{cross} which represents the mass per unit length was used to equate the d_{ae} for different fibre lengths. It showed that asbestos with $\rho A_{\text{cross}} = 300$ had no variation in d_{ae} while carbon fibre with $\rho A_{\text{cross}} = 19,390$ did.

Acknowledgement

The financial support provided by the Australian Research Council (Project ID LP0561870) is gratefully acknowledged.

References

Balásházy, I., Hofmann, W., & Heistracher, T. (2003). Local particle deposition patterns may play a key role in the development of lung cancer. *Journal of Applied Physiology*, *94*, 1719–1725.

Cheng, Y. S., Holmes, T. D., Gao, J., Guilmette, R. A., Li, S., Surakitbanharn, Y. et al. (2001). Characterization of nasal spray pumps and deposition pattern in a replica of the human nasal airway. *Journal of Aerosol Medicine*, *14*(2), 267–280.

Clift, R., Grace, J. R., & Weber, M. E. (1978). *Bubbles, drops, and particles*. London: Academic Press.

Crowder, T. M., Rosati, J. A., Schroeter, J. D., Hickey, A. J., & Martonen, T. B. (2002). Fundamental effects of particle morphology on lung delivery: Predictions of Stokes law and the particular relevance to dry powder inhaler formulation and development. *Pharamaceutical Research*, *19*, 239–245.

Finck, M., Hänel, D., & Wlokas, I. (2006). Simulation of nasal flow by lattice Boltzmann methods. *Computers in Biology and Medicine*, *37*, 739–749.

Gabitto, J., & Tsouris, C. (2007). Drag coefficient and settling velocity for particles of cylindrical shape. *Powder Technology*. doi:10.1016/j.powtec.2007.07.031.

Hahn, I., Scherer, P. W., & Mozell, M. M. (1993). Velocity profiles measured for airflow through a large-scale model of the human nasal cavity. *Journal of Applied Physiology*, *75*, 2273–2287.

Haider, A., & Levenspiel, O. (1989). Drag coefficient and terminal velocity of spherical and nonspherical particles. *Powder Technology*, *58*, 63–70.

Inthavong, K., Tian, Z. F., Li, H. F., Tu, J. T., Yang, W., Xue, C. L., & Li, C. G. (2006). A numerical study of spray particle deposition in a human nasal cavity. *Aerosol Science and Technology*, *40*, 1034–1045.

Kelly, J. T., Asgharian, B. C., Kimbell, J. S., & Wong, B. A. (2004). Particle deposition in human nasal airway replicas manufactured by different methods. Part 1: Inertial regime particles. *Aerosol Science and Technology*, *38*, 1063–1071.

Keyhani, K., Scherer, P. W., & Mozell, M. M. (1995). Numerical simulation of airflow in the human nasal cavity. *Journal of Biomechanical Engineering*, *117*, 429–441.

Kreuzer, M., Muller, M. K., Brachner, A., Gerken, M., Grosche, B., Wiethege, T. et al. (2000). Histopathologic findings of lung carcinoma in German uranium miners. *Cancer*, *89*, 2613–2621.

Lippman, M. (1990). Effects of fibre characteristics on lung deposition, retention and disease. *Environmental Health Perspectives*, *88*, 311–317.

Pattle, R. E. (1961). The retention of gases and particles in the human nose. In C. N. Davies (Ed.), *Inhaled particles and vapors* Oxford, UK: Pergamon Press.

Shi, H., Kleinstreuer, C., Zhang, Z. (2006). Laminar airflow and nanoparticle or vapor deposition in a human nasal cavity model. *Journal of Biomechanical Engineering*, *128*, 697–706.

Stöber, W. (1972). Dynamic shape factors of nonspherical aerosol particles. In T. Mercer et al. (Eds.), *Assessment of airborne particles* (pp. 249–289). Springfield, IL: Charles C. Thomas.

Su, W. C., & Cheng, Y. S. (2005). Deposition of fiber in the human nasal airway. *Aerosol Science and Technology*, *39*, 888–901.

Subramaniam, R. P., Richardson, R. B., Morgan, K. T., & Kimbell, J. S. (1998). Computational fluid dynamics simulations of inspiratory airflow in the human nose and nasopharynx. *Inhalation Toxicology*, *10*, 473–502.

Sussman, R. G., Cohen, B. S., & Lippmann, M. (1991). Asbestos fiber deposition in human tracheobronchial cast. I—Experimental. *Inhalation Toxicology*, *3*, 145–160.

Swift, D. L., & Proctor, D. F. (1977). Access of air to the respiratory tract. In J. D. Brain, D. F. Proctor, & L. M. Reid (Eds.), *Respiratory defence mechanisms* (pp. 63–93). New York, NY: Marcel Dekker.

Timbrell, V. (1982). Deposition and retention of fibres in the human lung. *Annals of occupational Hygiene*, *26*, 347–369.

Tran-Cong, S., Gay, M., & Michaelides, E. E. (2004). Drag coefficients of irregularly shaped particles. *Powder Technology*, *139*, 21–32.

Wadell, H. (1933). Sphericity and roundness of rock particles. *Journal of Geology*, *41*, 310–331.

WHO. (2000). Man-made vitreous fibres. In *Air quality guidelines*, 2nd ed., Chapter 8.2. World Health Organization.

Zamankhan, P., Ahmadi, G., Wang, Z., Hopke, P. K., Cheng, Y. S., Su, W. C. et al. (2006). Airflow and deposition of nano-particles in a human nasal cavity. *Aerosol Science and Technology*, *40*, 463–476.